Optical Materials 142 (2023) 114081

Contents lists available at ScienceDirect

Optical Materials

journal homepage: www.elsevier.com/locate/optmat

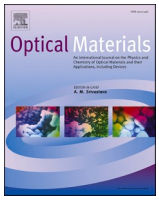

Research Article

Crystalline S-doped TiO_2 photoanodes from amorphous titanium oxysulfide (TiO_xS_y) for photo-oxidation reactions

Daniel R.S. Pitombeira [a], Maria J.S. Costa [b], Renato A. Antunes [c], Raphael O. Ferreira [d], Rejane M.P. Silva [a,e], Reginaldo S. Santos [a,*]

[a] Department of Chemistry-PPGQ, State University of Piauí - UESPI, Campus Poeta Torquato Neto, Pirajá, Teresina, 64002-150, PI, Brazil
[b] Department of Chemistry-PPGQ, Federal University of Piauí – UFPI, Campus Ministro Petrônio Portella – Ininga, Teresina, CEP: 64049-550, PI, Brazil
[c] Center for Engineering, Modeling and Applied Social Sciences - Federal University of ABC/UFABC, Bangu, Santo André, 09210-580, SP, Brazil
[d] Department of Mechatronics and Mechanical Systems Engineering - Poli/USP, Butantã, São Paulo, 05508-010, SP, Brazil
[e] Institute for Energy and Nuclear Research - IPEN/CNEN, Cidade Universitária, São Paulo, 05508-000, SP, Brazil

ARTICLE INFO

Keywords:
S-doped TiO_2 film
Titanium oxysulfide
Photoelectrochemistry
Photo-oxidation reactions

ABSTRACT

S-doped TiO_2 films were prepared by oxidation annealing of amorphous titanium oxysulfide (TiO_xS_y) at different temperatures. According to the X-ray diffraction patterns, the films calcined at temperatures of 300–600 °C showed only anatase phase, while the uncalcined sample was amorphous. The chemical composition of synthesized TiO_xS_y was estimated by X-ray photoelectron spectroscopy (XPS). High-resolution S 2p spectra showed S^{-2} bonds at 163.47 eV for the amorphous sample. The intensity of this signal decreased after heat treatment. Raman spectroscopy indicated an organization of the material structure with heat treatment of the material. Furthermore, optical characterization revealed that sulfur as dopant into the anatase TiO_2 structure, shifted light absorption from ultraviolet to the visible region. Photoeletrochemical studies developed under polychromatic irradiation revealed superior photocurrents for samples calcined at 600 °C, with *n*-type behavior, adequate for photo-oxidation reactions.

1. Introduction

Titanium dioxide (TiO_2) is still the most investigated semiconductor oxide due to its great photocorrosion stability and relatively low cost. Thus, thin TiO_2 films are largely used for solar energy conversion, including solar cells, water disinfection by photocatalytic removal of organic pollutants and solar hydrogen generation [1–5]. However, the wide band gap energy (E_{BG}) of 3.2 eV limits the TiO_2 photoactivity to UV irradiation, that corresponds to less than 5% of sunlight [6,7]. Thus, attention has been paid to modify the optical property of TiO_2 employing physical and chemical strategies that include the doping with metals or non-metals elements, and the adsorption of semiconductor nanoparticles of smaller band gap energy. In this regard, chemical strategies play a major role, including doping with metal or non-metal elements, and the adsorption of semiconductor with smaller band gap energy, forming a heterojunction [8]. In general terms, these strategies are efficient to improve the visible light harvesting by TiO_2.

The introduction of an impurity into the TiO_2 structure may reduce E_{BG} value due to the formation of intermediate energy levels, which are formed between the valence band (VB) and the conduction band (CB) [9]. In addition to reducing E_{BG}, the dopant creates traps that reduce the rate of recombination of electron/hole (e^-/h^+) charges, formed during semiconductor irradiation. The doping of many oxides can be achieved using different methodologies, such as Chemical Vapor Deposition (CVD) [10], Sputtering [11], Sol-Gel [12], Hydrothermal [13] and Solid-State Reaction [14]. The dopant can be a metal or non-metal, and depending on the method and synthesis conditions, during doping, an unwanted deleterious phase can be formed [15]. For example, Fe doping of TiO_2 may lead to the formation of hematite (Fe_2O_3) [16]. However, deleterious phase formation is not registered for non-metal doping such as N, C and S. Thus, the doping of TiO_2 with non-metals has been investigated as an option to obtain one single oxide phase. The S atom as a dopant has been investigated as the best non-metal alternative for the reduction of E_{BG} from TiO_2, because its ion can present an oxidation state ranging from S^{2-} to S^{6+}. There are two possible positions for sulfur as impurity into the TiO_2 structure, interstitial or substitutional positions. Thus, sulfur can replace titanium or oxygen when substitutional doping is considered. Studies show that S^{4+} or S^{6+} can occupy Ti sites in

* Corresponding author.
E-mail address: rsantos.uespi@gmail.com (R.S. Santos).

https://doi.org/10.1016/j.optmat.2023.114081
Received 10 May 2023; Received in revised form 14 June 2023; Accepted 26 June 2023
Available online 6 July 2023
0925-3467/© 2023 Elsevier B.V. All rights reserved.

cationic doping, while S^{2-} are observed in oxygen sites for anionic doping [17,18].

There are many routes to prepare S-doped TiO_2 (S-TiO_2), including hydrothermal, sol-gel, spray pyrolysis and thermal CVD [12–21]. Most S-TiO_2 preparation methods employ titanium thiourea and Titanium Isopropoxide (TTIP) as sources of S and Ti, respectively, which results in cationic doping. Considering these synthesis methodologies, it is impossible to obtain S-TiO_2 with anionic doping, because the ionic radius of S^{2-} (1.7 Å) is greater than that of O^{2-} (1.22 Å). Furthermore, the Ti-O (673 kJ mol^{-1}) binding energy of TTIP precursor is too large to be disrupted for further Ti-S (418 kJ mol^{-1}) bond formation [22]. Thus, the preparation of S-TiO_2 with sulfur in the anionic doping can be achieved through the heat treatment of TiS_2 in an oxidizing atmosphere, converting the sulfide into TiO_2. This chemical transformation leaves residual S atoms in the TiO_2 structure, which act as anionic dopants of the crystalline semiconductor lattice [23].

About 20 years ago, Umebayashi et al. [24] developed important studies with the conversion of TiS_2 into S-TiO_2, with subsequent photocatalytic application in the degradation of methylene blue under visible irradiation [25]. Since then, intense research has been carried out aiming at the optical modification of TiO_2, with a view to its application in photocatalysis under visible light. For instance, Wang et al. [26] investigated S-doped TiO_2 prepared from TiS_2 employing hydrothermal method, and observed a superior catalytic activity for degradation of Rhodamine B (RhB) under visible light. Similarly, Jing et al. [27] synthesized anatase TiO_2 nanosheets by chemical oxidation of TiS_2 and investigated its photocatalytic activity for methylene blue solution discoloration under UV irradiation. However, the preparation of pure TiS_2, used as a precursor of TiO_2 doped with sulfur, requires special synthesis conditions, which include high temperatures, purity of reagents and inert atmosphere. To prepare S-doped TiO_2, the synthesized TiS_2 is usually placed in an oxidizing atmosphere. On the other hand, the synthesis of titanium oxysulfide (TiO_xS_y) requires milder synthesis conditions. Likewise, TiO_xS_y can be used as a precursor material for the preparation of S-doped TiO_2, with sulfur atoms occupying oxygen sites. However, there are no reports on the thermal conversion of TiO_xS_y into sulfur-doped TiO_2.

Titanium oxysulfide (TiO_xS_y) is a compound formed only by titanium, oxygen and sulfur atoms in its structure. In this compound, the oxidation states for the anions must be O^{2-} and S^{2-}. Amorphous TiO_xS_y was first reported by Meunier et al. [28], who prepared the material from radiofrequency sputtering using a TiS_2, target and controlled amounts of oxygen. More recently, Smith et al. [29] investigated the synthesis of titanium oxysulfide from mesoporous TiO_2 and hexamethyldisilathiane. The authors studied the electrical conductivity for material prepared in different synthesis condition. Also, Kasteren et al. [30] reported about conductivity of TiO_xS_y thin film prepared by Atomic Layer Deposition (ALD) technique, and presented XPS signal for S 2p indicating only the S^{2-} oxidation state for sulfur, characteristic of titanium oxysulfide.

In many studies on photocatalytic activity of semiconductor oxides for organic pollutants degradation, the semiconductor material is dispersed as powder in the catalytic reactor. However, our studies have shown that the photoelectrocatalytic degradation of organic species in solution can be improved with the catalyst material supported in the form of films, which allows the application of the bias potential (photoelectrocatalysis) [31–33]. The potential applied to the photocatalytic system helps in the charge separation process, reducing the recombination rate of the e^-/h^+ pair and increasing the reaction efficiency [34,35].

In this work, we synthesized amorphous TiO_xS_y and prepared films on a transparent conductive substrate. To convert the TiO_xS_y into S-doped TiO_2, the films were calcined in an oxidizing atmosphere at different temperatures. The initial TiO_xS_y sample chemical composition was determined by X-ray photoelectron spectroscopy (XPS) analysis. Furthermore, X-ray diffraction (XRD) and UV–vis absorption spectroscopy were carried out in order to verify the thermal treatment effect on structural and optical properties of the samples. To the best of our knowledge, the S-doped TiO_2 films prepared from chemical oxidation of TiO_xS_y and consequent photoelectrochemical study of the electrodes has not yet been reported.

2. Materials and methods

2.1. Synthesis of TiO_xS_y and photoelectrodes preparation

TiO_xS_y particles were prepared based on methodology described by Prabakar et al. [36]. Briefly, the reaction was performed in a three-neck round-bottom flask by dissolving 0.192 g of elemental sulfur in 20 mL of octadecene (90%, Aldrich) and heating to 220 °C. After complete dissolution of elemental sulfur, 1.0 mL of titanium tetrachloride ($TiCl_4$ 98.5%, Aldrich) was added and a solid black precipitate was formed. The black solid was centrifuged and washed with toluene to remove reaction byproducts. During synthesis, the system was placed in silicone oil bath and purged with N_2 atmosphere.

Suspension formed from the black solid material obtained during the syntheses, 40% (w/w) Polyethylene glycol 20,000 (PEG 20000-Aldrich), and 5% (w/w) of Triton X-100 (Sigma-Aldrich) was utilized to prepare the films by doctor-blade methodology. The films were prepared on a transparent conductive substrate, formed by a layer of Fluorine-doped Tin Oxide (FTO), with resistivity of 8 Ω/sq deposited on glass, which represents a conductivity of 0.125 $(\Omega/sq)^{-1}$. In order to simplify, in this current work, we named the substrate just as FTO-glass. The FTO-glass was cut in dimension of 1.0 × 2.5 cm^2 and the ultrasonic cleaning of the glasses occurred in three stages: deionized water with detergent, isopropyl alcohol, and deionized water, respectively, each for 15 min. Next, photoelectrodes were prepared by depositing in FTO-glass, and the films were subsequently calcined at different temperatures from 300 °C to 600 °C for 2 h.

2.2. Composition, thermal properties, structural, morphological and optical characterization of the samples

X-ray Photoelectron Spectroscopy (XPS, K-alpha + model, Thermo Fisher Scientific, operating with Al-kα radiation source) was used to investigate the elemental composition, chemical and electronic state of the elements present on the surface of the samples as prepared and calcined at different temperatures. The pressure in the analysis chamber was approximately 10^{-7} Pa and spot size was 400 μm. For the survey and high-resolution XPS spectra, the pass energies were 50 eV and 20 eV, respectively. Thermogravimetric analysis (TGA) and Differential scanning calorimetry (DSC) measurements were carried out in the simultaneous equipment (model TG-50, Shimadzu), in synthetic air with flow of 50 mL min^{-1}, heating rate of 5 °C min^{-1}, and temperature range of 25–600 °C. Powder X-ray diffraction (XRD) was utilized for structural characterization of TiO_xS_y and calcined films at different temperatures. The XRD patterns were registered on LabX XRD-6000 diffractometer (Shimadzu, Japan) equipment using CuKα (λ = 0.15406 nm) radiation. The intensity data were collected over a 2θ range of 10°–80° with scan rate 1°.min^{-1} and the X-ray patterns of the samples were compared with the Joint Committee on Powder Diffraction Standards (JCPDS) cards. The morphology and elemental analysis were characterized by Scanning Electron Microscopy (SEM) coupled to the Energy Dispersive X-ray Spectrometer (EDS) (JEOL EDS System, model 6010LA) with acceleration voltage between 0.5 and 30 kV.

Raman spectroscopy analysis was carried out using a SENTERRA (Bruker, Germany) spectrometer, as excitation source, a 532 nm laser He-Ne was used, with nominal power of 0.2 mW. Measurements were taken between 85 and 100 cm^{-1}, with spectral resolution of 3 cm^{-1}. The optical properties of the films were assessed through spectroscopy in the UV–Vis region, using $BaSO_4$ as a reference in the Shimadzu UV-2600 spectrophotometer. The value of the optical band gap energy of the

films was estimated by the Kubelka-Munk function from the UV–Vis transmittance curves [37].

2.3. Photoelectrochemical characterization

For electrochemical characterization, voltammetric experiments were performed using a potentiostat–galvanostat (Autolab PGSTAT 302-N Metrohm). The photoelectrodes were characterized by chronopotentiometry (CP), cyclic voltammetry (CV), chronoamperometry (CA) and Electrochemical Impedance Spectroscopy (EIS) using a Na_2SO_4 0.5 mol L^{-1} aqueous solution as the supporting electrolyte and a three-electrode cell: a saturated Ag/AgCl electrode, platinum wire, and TiO_xS_y or S-TiO_2 photoelectrodes as the reference, counter-electrode and working electrodes, respectively. EIS results (Nyquist and Mott–-Schottky plots) of calcined films were registered at applied open circuit potential (OCP), with frequencies ranging from 1 Hz to 1 MHz and AC amplitude of 10 mV.

The electrochemical studies were developed employing a polychromatic metal vapor lamp (HQI-TS NDL - 150 W) setting for 100 mW cm^{-2} as irradiation source. For comparison effect, all values obtained with the Ag/AgCl reference were converted to the Normal Hydrogen Electrode (NHE) potential, according to Eq. (1) [31]:

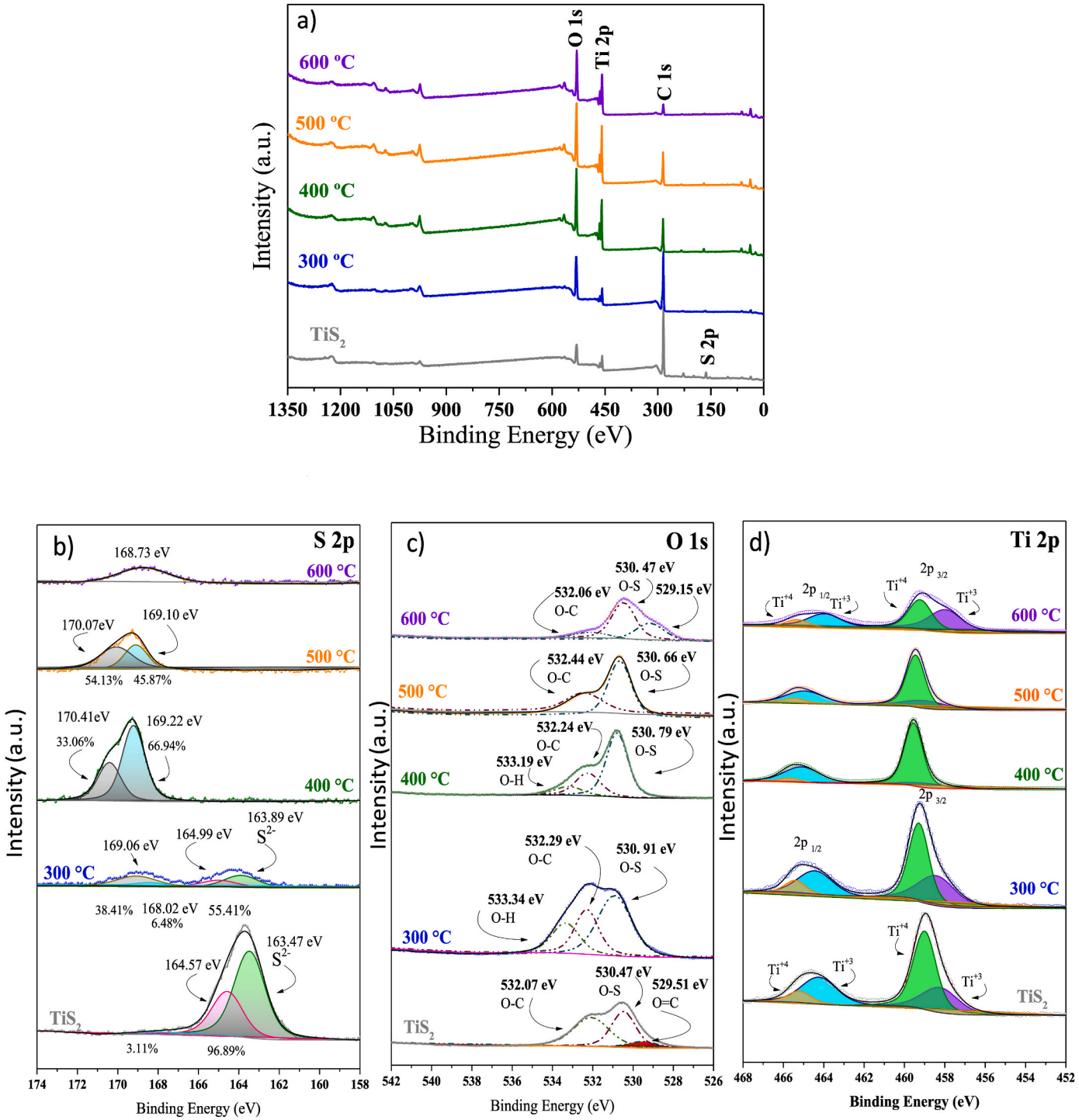

Fig. 1. XPS spectrum: (a) Survey of amorphous TiO_xS_y and calcined samples; High-resolution core levels spectra for (b) Ti 2p; (c) O 1s and (d) S 2p orbitals.

$$E\ (vs,\ NHE) = E\ (vs,\ Ag/AgCl) + 0.0591V\ x\ pH + 0.199\ V \quad \text{Eq. (1)}$$

Also, the potentials after adjusted to the NHE (in volts) were converted in electron-volts (eV) based in equation (2),

$$E(eV) = [-4.5\ eV - eE_{(NHE)}] \quad \text{Eq. (2)}$$

where (e) is the electron charge.

3. Results and discussion

3.1. Chemical composition, thermal, structural and optical characterizations

XPS analysis was performed in order to determine the chemical composition and the chemical states of elements present on TiO_xS_y and calcined samples. Fig. 1 shows XPS results obtained for calcined samples in comparison to initial material. The survey spectrum, Fig. 1a, shows characteristic XPS signals of S, C, Ti and O for all samples. To determine the surface elemental composition from XPS analysis, the carbon signal was ignored and the results are summarized in Table 1. In a pure TiO_xS_y sample, the Ti composition is about 33%, while O is almost 67%. As observed from Table 1, after heat treatment, the Ti content increased to 30.03%, and O is 72.37%. Oxygen atoms present in the oxygenated species, formed as a by-product of the decomposition of titanium oxysulfide, can remain adsorbed to the surface of the material. Thus, overestimated oxygen content is expected in XPS analysis because this technique has a probing depth of up to 10 nm (surface-sensitive technique). However, the heat treated films have an O/Ti ratio that decreases with increasing temperature, reaching 2.26. This value is close to the expected for TiO_2 structure. Similarly, the ratio in atomic percentages of S/Ti tends to stabilize after heat treatment. As previously discussed, due to the overestimated amount of oxygen on the surface of the material, S-doped TiO_2 films present a value of $x + y > 2$. Similar results were observed in recent studies by Kasteren et al. [30].

Metal oxysulfides must have sulfur atoms with oxidation state S^{2-} [38]. The high-resolution S 2p XPS spectrum confirms titanium oxysulfide as an initial material for the preparation of S-doped TiO_2 electrodes. Fig. 1b shows XPS asymmetric peak for S 2p from the TiO_xS_y sample, which was deconvoluted into two sub peaks corresponding to S $2p_{3/2}$ and S $2p_{1/2}$. These signals located at 163.47 and 164.57 eV (ΔE = 1.10 eV) can be assigned to the Ti-S bonds for TiO_xS_y sample [39]. The binding energy of 163.89 eV of the S^{2-} ions still occurs in the calcined sample at 300 °C. However, this signal is almost zero for samples calcined at 400, 500 and 600 °C. The drastic reduction in the signal attributed to the S^{2-} ions suggests that from 400 °C almost all the sulfur in the initial structure of the amorphous TiO_xS_y was replaced by oxygen atoms, leading to the formation of TiO_2 in the anatase phase with some S atoms as impurities. The result found here is similar to that presented by Umebayashi et al. [24], in studies of conversion of crystalline TiS_2 into S-doped TiO_2. The S^{6+} and S^{4+} signals present in the XPS spectra at around BE 170.50 eV can be associated with the formation of SO_4^{2-} and SO_2^- species as by-products of the amorphous TiO_xS_y thermal decomposition reaction.

Fig. 1c shows the high-resolution O 1s XPS spectrum obtained for all samples. The signal was deconvoluted into three peaks ranging from 529.51 to 533.19 eV, which can be attributed to lattice oxygen of TiO_2 or non-reticular oxygen [40]. For sample of amorphous TiO_xS_y, the signals at 529.51, 530.47 and 532.07 can be attributed to oxygen bound to carbons belonging to precursors of synthesis. This result suggests that even under conditions of purging the reaction system with nitrogen gas, oxygen was incorporated into the material during synthesis. The XPS peak with a maximum at approximately 530.47 eV is attributed to lattice oxygen of TiO_2, while the signal at higher BE values is attributed to adsorbed species or the effect of oxygen vacancies.

High-resolution Ti 2p spectra displays two well defined peaks (doublet) with average binding energy (BE) of 459.44 eV and 465.23 eV, attributed to Ti $2p_{3/2}$ and Ti $2p_{1/2}$, respectively (Fig. 1d). For all samples, the Ti 2p XPS peaks are formed by contributions from Ti^{3+} and Ti^{4+} [41,42]. The lowest oxidation state for the titanium ion must occur due to oxygen vacancies present in the structure of the calcined material. The presence of Ti^{3+} can be attributed to defects caused by the absence of sulfur or oxygen atoms. Furthermore, Ti 2p XPS peaks were shifted to higher BE values, indicating that the chemical environment of the titanium atom changed with heat treatment.

According to the XPS analysis, in samples calcined at 400, 500 and 600 °C, almost all the sulfur atoms were replaced by oxygen atoms, leaving some sulfur atoms as an impurity (doping) in substitutional positions to the oxygen atoms, resulting in S-doped TiO_2 sample.

The effect of heat treatment on films was investigated by thermal analysis techniques.TGA and DSC studies were carried out for the suspensions used in the preparation of films (see experimental Section). Fig. 2 shows TGA/DSC curves registered for sample in oxidizing atmosphere. From TGA analysis, it is possible to observe a mass loss of 97% at temperatures between 70 and 90 °C, followed by a second mass loss of ca. 2.0%. Considering the endothermic signal in DSC curve, the first thermal event is attributed to water elimination, while the second weight loss is associated to octadecene and PEG decomposition, occurred at 185 and 324 °C, respectively. From 320 °C a residual mass of about 1% was registered in TGA curve. The TGA curve for the as-prepared TiO_xS_y sample revealed a mass loss even after 320 °C, which must still be associated with the elimination of residual octadecene from the material. Previous studies made by DSC registered a phase change of TiO_2 from amorphous to crystalline (anatase) in a temperature range from 250 to 430 °C [43]. Thus, the DSC signal, with a maximum centered at 324 °C, may also have contributions from the phase transition of the material. Also, a change in the baseline from 503 °C may be associated with a greater organization of the material structure. In order to confirm this phase transition from TiO_xS_y to TiO_2 phase, a structural characterization of the material calcined in temperatures de 300 to 600 °C was carried out using the X-ray diffraction (XRD) technique.

Table 1
Composition of the TiO_xS_y and S-doped TiO_2 estimated from XPS survey spectra.

Sample	% Ti	% O	% S	O/Ti (x)	S/Ti (y)
As prepared	17.44	65.03	17.53	3.73	1.01
300 °C	11.62	84.93	3.44	7.31	0.30
400 °C	23.64	72.16	4.19	3.05	0.18
500 °C	25.29	72.37	2.34	2.86	0.09
600 °C	30.03	67.97	2.00	2.26	0.07

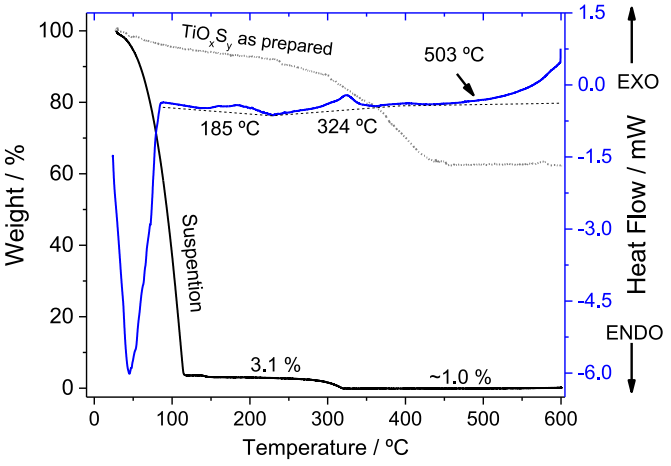

Fig. 2. Thermogravimetric Analysis (TGA) and Differential Scanning Calorimetry (DSC) curves for suspension prepared from $TiCl_4$ and sulfur, obtained in synthetic air airflow.

Fig. 3 shows the X-ray diffraction pattern for the sample calcined at different temperatures. Although the material shows a dark coloration, characteristic of TiO_xS_y, the absence of diffraction signals for the as-prepared sample indicates that the material is predominantly amorphous. However, with the thermal treatment, the samples treated at 300–600 °C show diffraction signals in concordance with JCPDS n° 84–1286 card, corresponding to TiO_2 in anatase phase. Commercial TiO_2 was used as a standard for comparison in XRD measurements. As can be seen, the JCPDS card of TiO_2 in the anatase phase is in perfect agreement with the pattern XRD. Also, no deleterious phase or other structure for TiO_2 was observed.

As predicted in the DSC curves, the exothermic signals that occurred for temperatures above 300 °C could also be associated with the phase transition of the material. XRD patterns indicated that this transition initially occurred from amorphous TiO_xS_y to anatase TiO_2 at 300 °C. The sample treated at 600 °C presents more intense and well-defined diffraction signals, exhibiting a superior organization of the oxide crystals. Furthermore, the broad diffraction signals for the samples heat treated at 300, 400 and 500 °C suggest that the material is formed by nanoparticles. Thus, at 600°, the diffractogram suggested that due to the heat treatment, the nanoparticles aggregate, forming larger crystals [44].

Fig. 4 shows Raman spectra for materials calcined at different temperatures. The results indicate that amorphous TiO_xS_y was transformed into crystalline anatase during heat treatment. Anatase phase displays 15 optical modes, and six of these modes represented by $1A_{1g}$, $2B_{1g}$ and 3 Eg are active in Raman [45,46]. Fig. 4 shows Raman spectra with five signals attributed to E_g (145 cm^{-1}), B_{1g} (197 cm^{-1}), A_{1g} (396 cm^{-1}), B_{1g} (516 cm^{-1}) and E_g (639 cm^{-1}) modes of the TiO_2 anatase phase.

As previously noticed from the XRD results, the Raman signals indicate an organization of the oxide structure with heat treatment of the material. Studies with chemical oxidation of TiO_xS_y show that the formed TiO_2 also presents sulfur atoms in the structure, occupying oxygen sites, corresponding to a substitutional anionic doping. The dopant can change the electronic and optical properties of the material. Thus, optical studies with UV–Vis measurements had already suggested that the presence of S^{2-} ions as impurities changed the semiconductor E_{BG}, improving its ability to absorb radiation with longer wavelengths. The electronic alteration caused by the dopant must change the electrochemical properties of the films prepared from the synthesized material.

Fig. 5 shows optical characterization for calcined samples developed by UV–Vis spectroscopy in Reflectance mode. With the exception of the sample treated at 300 °C, from the UV–Vis curves registered in Fig. 5a,

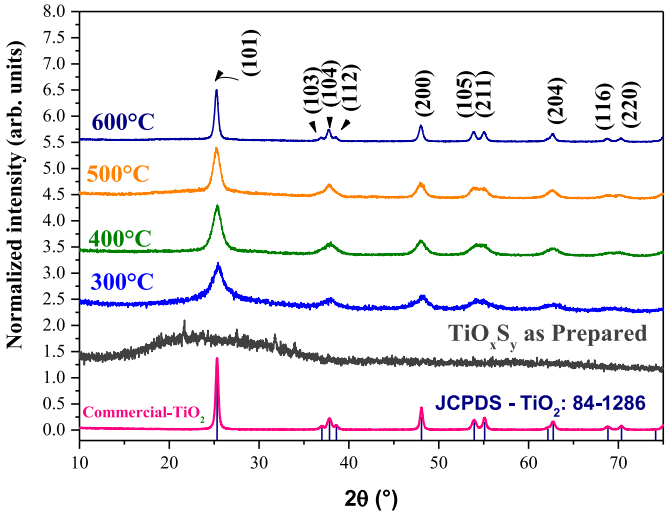

Fig. 3. XRD diffraction patterns obtained for untreated sample and after thermal treatment at different temperatures.

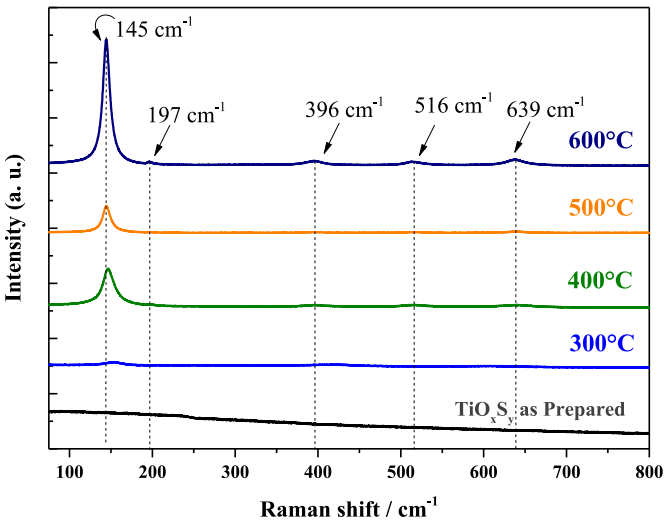

Fig. 4. Raman spectra of as prepared TiO_xS_y in comparison to sample treated at 300, 400, 500 and 600 °C during 120 min.

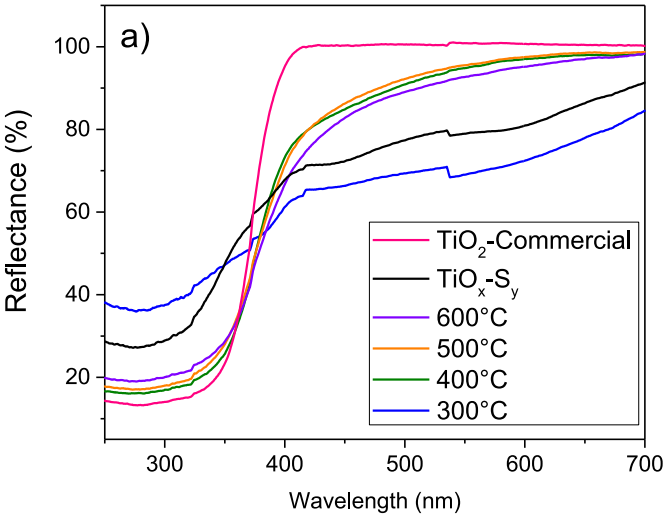

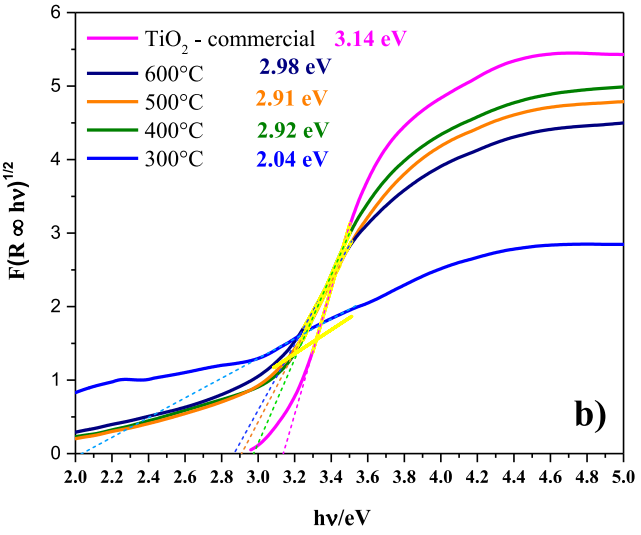

Fig. 5. (a) UV–Vis curves for amorphous TiO_xS_y and calcined powders, in comparison to commercial-TiO_2, registered in Reflectance mode; and (b) E_{BG} values estimated by Kubelka-Munk function for calcined samples.

we observe that commercial-TiO_2 UV–Vis curve presents a percentage reflectance (%R) of almost 100% from 700 to about 400 nm. All other curves recorded for samples prepared from TiO_xS_y show %R values lower than one hundred percent. The samples calcined at 600, 500 and 400 °C present similar %R values, with absorption at wavelengths in the visible range of the spectrum. The lower %R for the film treated at 300 °C is probably due to the partial contribution of amorphous TiO_xS_y still present in the sample. For amorphous TiO_xS_y sample, a greater absorption of light in the visible range was recorded, probably, due to the dark color of the initially synthesized material. This result suggests that from 400 nm, light can promote electrons from the valence band, overcoming the band gap energy of the crystalline materials prepared from amorphous TiO_xS_y sample. From UV–Vis curves, the optical band gap energy, E_{BG}, was estimated by Kubelka-Munk function [47]. The curves shown in Fig. 5b suggest indirect transition energies of 2.04, 2.92, 2.91 and 2.98 eV for the samples calcined at 300, 400, 500 and 600 °C, respectively. As the XRD and Raman data showed that TiO_xS_y is not crystalline, the E_{BG} value was not estimated from its UV–Vis curve.

Fig. 6 shows representative SEM images with the morphology, mapping and EDS spectra of films prepared on transparent conductive substrate. As registered in the EDS mapping, the films are formed by a homogeneous distribution of Ti, O and S elements on the surface of the samples. In addition, the films have an irregular morphology formed by pores and cracks that are formed during heat treatment (Fig. 6a–b). This morphology is probably due to the elimination of organic components present in the suspension, such as PEG 20000 and Triton X-100. The EDS spectra shown in Fig. 6c–d reveal that heat treatment induced a reduction in the carbon (0.277 eV) and sulfur (2.31 eV) signals intensity. This result agrees with that one registered in XPS measurements, which indicated a reduction in the composition of sulfur atoms with consequent adjustment to stoichiometric proportions close to those expected for the TiO_2 phase. Comparative SEM images with the surface morphologies of the S-doped TiO_2 film and bare FTO-glass can be seen in Fig. 1S (Supporting Information). From Fig. 1S SEM image it is possible to perceive the formation of the titanium oxide film on the conductive substrate.

Electrochemical measurements of films can provide important information on charge transfer properties for the use of films as photoelectrodes. Fig. 7 shows chronopotentiometry curves recorded in dark-light intervals, in OCP condition. In the first hundred seconds of analysis, the electrochemical system is in the dark and there is only a balance of charges at the electrolyte-electrode interface. After irradiation (light on), there is electrons transition from VB to CB of the material. In the OCP condition, there is no flow of electrons towards the counter electrode and, therefore, there is an accumulation of charges in the CB of the semiconductor. The films calcined at 400, 500 and 600 °C present higher values in the photopotential variation, in light-dark conditions. The negative values for photopotential ($\Delta E <$ zero) are characteristic of *n*-type semiconductor. However, only films treated at 500 and 600 °C reach a steady state of potential right after irradiation. This result suggests that oxides calcined at lower temperatures present defects (traps), which generate localized levels between the VB and CB that impede the rapid transfer of electrons. Similarly, when irradiation is interrupted (light off), electrons return from CB to VB, which needs to overcome material defects. In this case, only the film calcined at 600 °C was able to reach the initial photopotential value, suggesting that the other electrodes need a longer time for the electrons to remain trapped in the intermediate energy levels. On the other hand, the TiO_xS_y film did not show photopotential, i.e., no photoelectrochemical response. This result indicates that the amorphous material film presents no charge

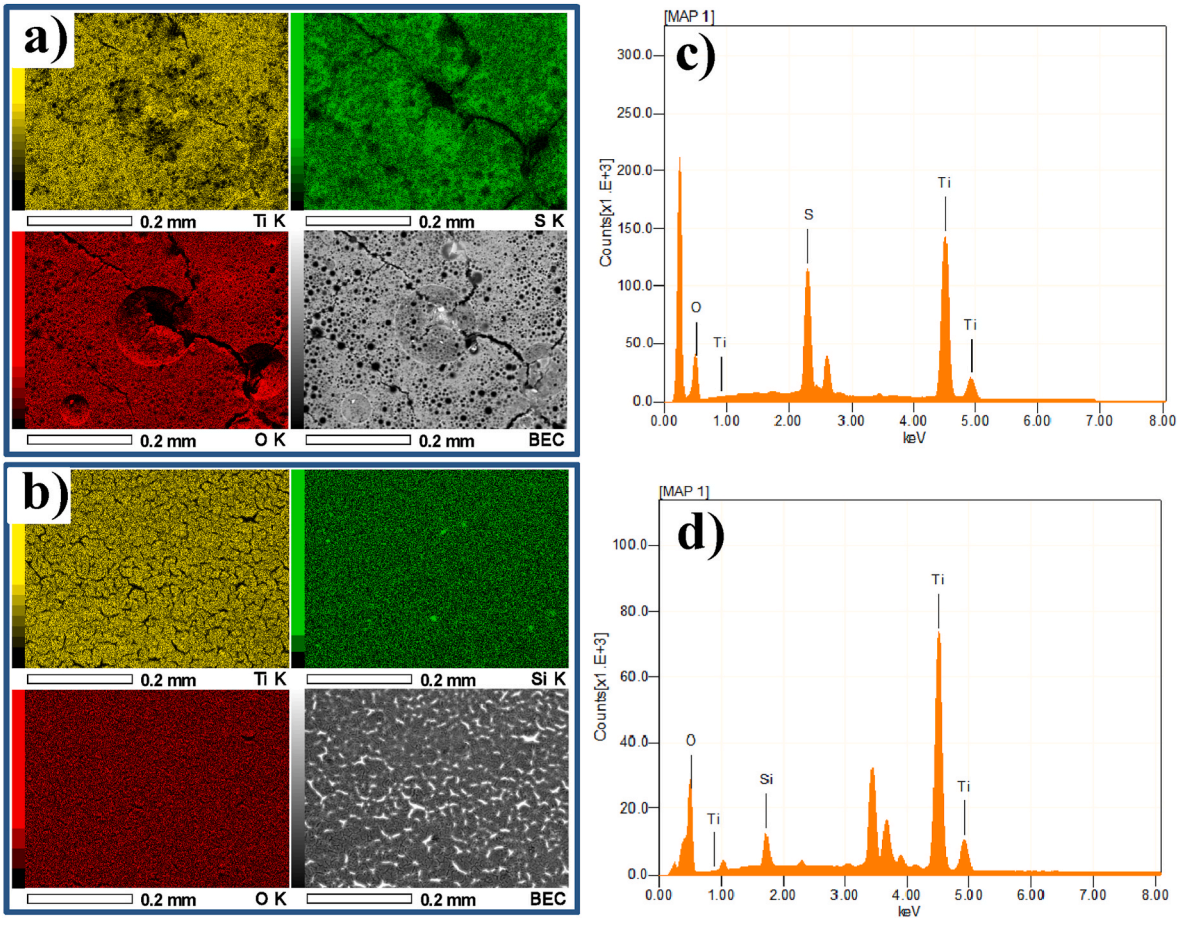

Fig. 6. EDS mapping and EDS spectra of (a,c) as prepared amorphous TiO_xS_y in comparison to (b,d) calcined film at 600 °C.

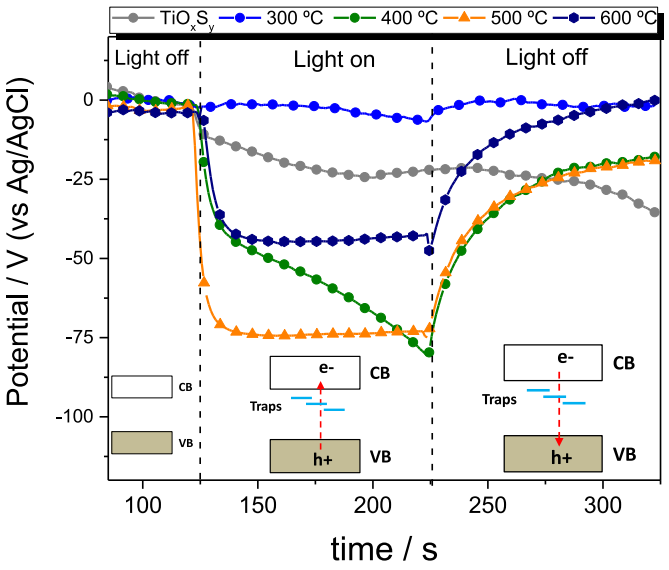

Fig. 7. The three-step Chronopotentiometric curves of TiO_xS_y and calcined films in the dark-light-dark interval under Open Circuit Potential condition (current zero).

separation and is not suitable for photoelectrocatalytic reactions.

Electrochemical Impedance Spectroscopy (EIS) is an important technique to evaluate the charge transfer resistance at the electrolyte-electrode interface. Fig. 8 displays EIS results of calcined films registered in 0.5 mol L^{-1} Na_2SO_4 solution (pH = 6.5). The charge transfer resistance responses observed on the Nyquist plots (Fig. 8) agree with the chronopotentiometry studies discussed earlier (see Fig. 7). The smaller circular radius in the high-frequency region of the electrode S-doped TiO_2 calcined at 600 °C indicates a lower charge transfer resistance and higher efficiency to electron diffusion in comparison to the film calcined at 300 °C (Fig. 8a). The results of the Mott–Schottky (M − S) analysis revealed conductivity *n*-type of calcined films as TiO_2-based material, typical of photoanodes. Mott–Schottky plots were obtained from the extrapolation of the flat band potentials (E_{fb}) of the photoanodes, according to Eq. (3):

$$\frac{1}{C^2} = \frac{2}{\varepsilon\varepsilon_0 A^2 e N_D}\left(E - E_{fb} - \frac{K_B T}{e}\right) \quad (3)$$

where C is the interfacial capacitance, *e* is the dielectric constant of the semiconductor, ε_0 is the permittivity of free space region, A is the area of the interfacial capacitance, N_D is the donor density, E is the applied potential, E_{fb} is the flat-band potential, K_B is the Boltzmann's constant, T is the temperature and e is the electronic charge. A plot of $\frac{1}{C^2}$ versus the potential produces a linear region. From the value of this slope, the E_{fb} of a semiconductor can be calculated and the intercept of the extrapolation of this linear plot to $\frac{1}{C^2} = 0$ gives its flat band potential. A positive slope indicates that the material is an *n*-type semiconductor and electrons are majority charge carriers. The slope of the tangent line, for fitting the Mott–Schottky curves, is in inversely proportional to the carrier density in the photoanode. These values were estimated between −0.18 and −0.04 V vs. Ag/AgCl. As for photoanode, Fermi energy is near CB, these E_{fb} values are attributed to CB. From these E_{fb} and E_{bg} values, it was possible assemble the relative positions of CB and VB in NHE and vacuum scale and determine the potential application as photoanodes in photoelectrocatalytic process (Fig. 8b).

Fig. 9 shows photoelectrochemical measurements recorded in the dark condition or under polychromatic irradiation of the electrodes, in addition to a schematic representation of the formation of the electrodes and their role in the photo-oxidation process. Fig. 9a shows that, in the dark, all electrodes displayed almost zero current values, in the potential range of 0.0–1.0 V (vs Ag/AgCl). Films treated at 300 and 400 °C presented very low photocurrent values, due to defects in materials structures. On the other hand, samples calcined at 500 and 600 °C presented superior photocurrent values because there is a greater organization of the crystalline structure and fewer defects. Photoelectrochemical analyzes were also carried out using K_2SO_4 0.5 mol L^{-1} solution, as the supporting electrolyte. The results showed that there is no significant difference in the current values obtained for Na_2SO_4 solution (see Fig. 2S - Supporting Information). XRD and Raman analysis have showed an amorphous phase for TiO_xS_y and less organization structure for samples calcined up to 400 °C. Thus, these electrochemical results corroborate data previously discussed on XRD and Raman analysis, which showed amorphous phase for TiO_xS_y and a higher crystallinity for films treated at 600 °C.

Fig. 9b presents chronoamperometric (CA) curves obtained for the film treated at 600 °C (S-doped TiO_2), under different pH conditions. From the CA curves it is possible to verify that the increase in the pH of the solution favors the charge separation process, resulting in higher currents. The negative charge of the OH^- present in the alkaline solution must react with the hole (h^+) photogenerated in the S-doped TiO_2 electrode. This result indicates that the alkaline medium reduces the electron/hole (e^-/h^+) recombination reactions and favors the photo-oxidation reaction that occurs on the electrode surface. Table 1S presented in Supporting Information shows that in addition to pH, there is a dependence of the crystalline phase, morphology, irradiation power and type of electrolyte on the photocurrent values recorded for films of TiO_2 doped with S.

In principle, the electron transport in porous electrodes depends on the connectivity of the crystalline particles composing the film. The model to explain the electron transport in porous electrodes of TiO_2 admits that when the electrode is immersed in the electrolyte, all particles come in to contact with the solution. In any particle, irradiation of light with $h\nu \geq E_{BG}$ results in electron-hole separation. If the reaction kinetics of the hole with the species present in solution is faster than the charge recombination process, the photogenerated electrons are transferred through the crystallites that constitute the film. In order to the electron can reach the conductive substrate and then be collected for the external circuit, the electron must be transferred through the colloidal particles and grain boundaries [48,49]. If the particles that form the film have low crystallinity or many defects, the charge transport mechanism is impeded as the defects act as traps for the charges. Thus, the photoelectrochemical behavior of the films prepared at different temperatures and the discussion presented in this present work contribute significantly to the understanding of the photocatalytic activity of S-doped TiO_2 electrodes in photo-oxidation reactions. Fig. 9c shows a representative diagram of the preparation of S-doped TiO_2 and the photo-oxidation mechanism that occurs in the particles of the material. Electrochemical measurements showed that S-doped TiO_2 is an *n*-type semiconductor. Therefore, electrons must be collected for the counter electrode, while holes must promote oxidation reactions of species present in the electrolyte.

4. Conclusions

Amorphous TiO_xS_y was prepared and calcined at four different temperatures. Analysis made by Differential Scanning Calorimetry (DSC) suggested that the material undergoes phase change up to 600 °C. XRD results revealed that with heat treatment the amorphous material becomes crystalline, with anatase phase. Raman spectra showed that there is a structural organization with the increase of the heat treatment temperature. XPS analysis showed that the films present the Ti 2p signal for Ti^{3+} and Ti^{4+}, associated with oxygen vacancies. Furthermore, the S 2p signal suggests S^{2-} for the as-prepared sample, which can be associated to the Ti–S bond in TiO_XS_y. However, S^{4+} and S^{6+} signals were observed for calcined samples, which may be associated with the formation of by-products such as SO_4^{2-} and SO_2 still attached to the surface

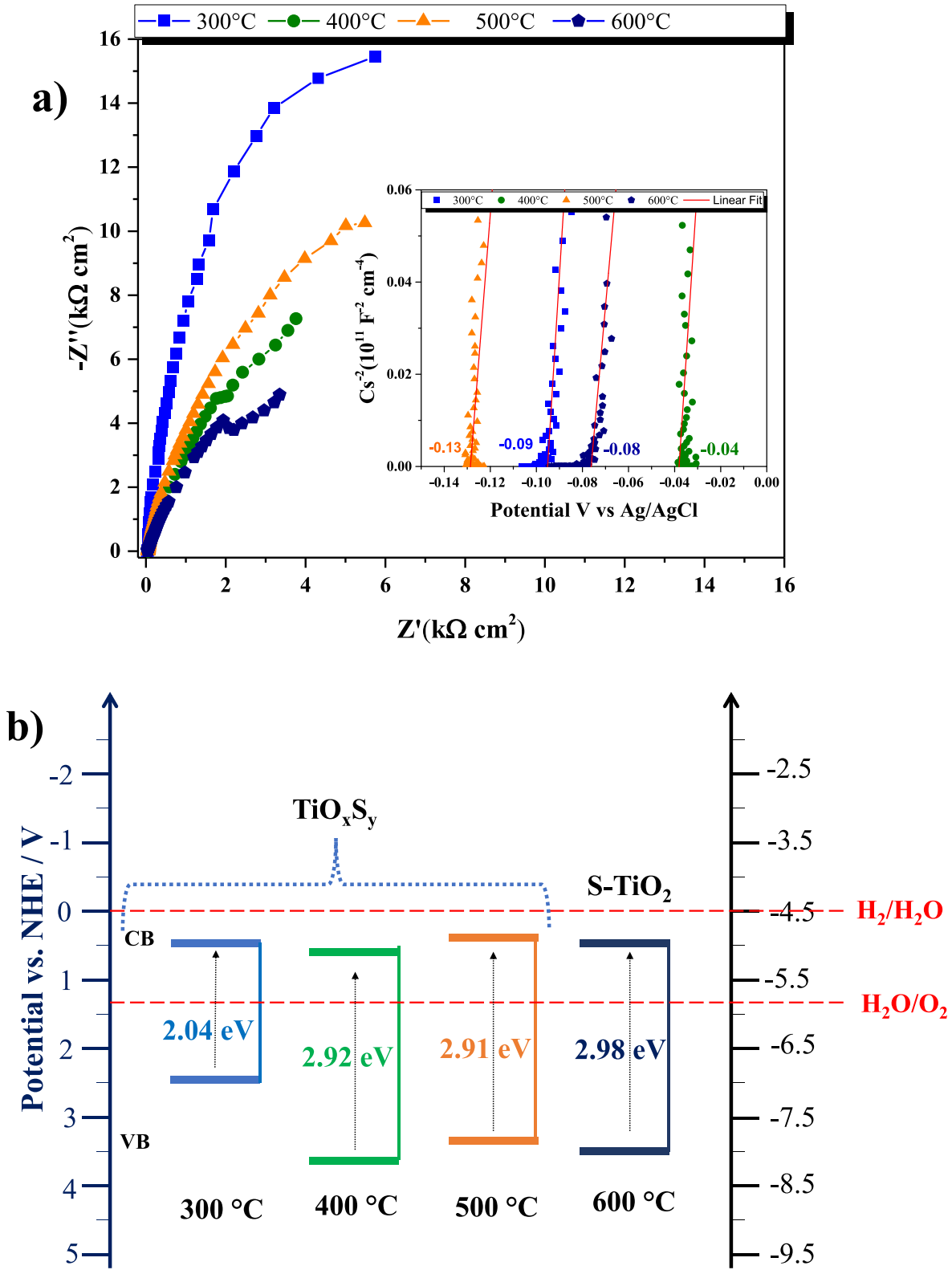

Fig. 8. (a) Nyquist plots of calcined electrodes obtained from amorphous TiO_xS_y in 0.5 mol L^{-1} of Na_2SO_4 solution and (b) Bands diagram for samples. Inset: Mott-Schottky plots with linear region corresponding to the flat band potential of the films.

of the materials. The remaining sulfur atoms in the TiO_2 anatase structure act as anionic substitutional dopants, occupying oxygen sites. Optical characterization showed that with increasing thermal treatment temperature, the doped TiO_2 films showed a shift in light absorption to the visible region. Photoelectrochemical studies revealed that materials calcined up to 400 °C have defects that act as traps for photogenerated charges. These electrodes presented *n*-type behavior and anodic photocurrent response for the studies carried out in inert electrolyte. The presented studies indicate that the doping of TiO_2 with sulfur atoms from the thermal oxidation of TiO_xS_y is an alternative to control the

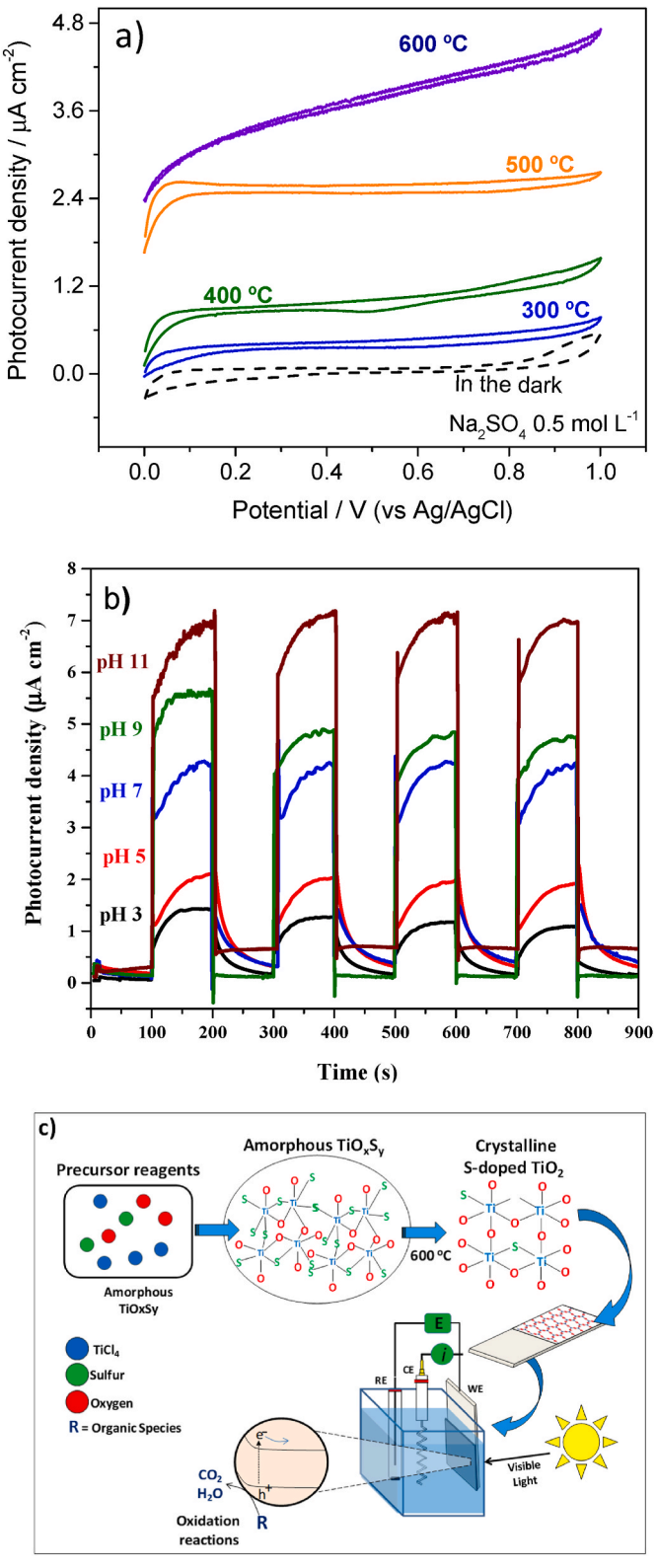

Fig. 9. (a) Cyclic voltammograms recorded at 20 mV s^{-1} for films obtained from amorphous TiO_xS_y calcined at different temperatures, in electrolyte Na_2SO_4 0.5 mol L^{-1}, (b) Chronoamperometry curves recorded in Britton-Robinson buffer solution with pH varying from 3 to 11, and (c) Schematic representation for the preparation of S-doped TiO_2 film and its catalytic activity for photo-oxidation reaction of species in solution.

position of S as dopant in the oxide structure. Thus, the S-doped TiO_2 film can be used as a photoelectrode to promote photo-oxidation reactions of organic species in aqueous medium, under polychromatic irradiation.

Credit authorship statement

Daniel R. S. Pitombeira: Conceptualization, Methodology, Investigation, Data curation, Writing – original draft, Writing – review & editing, Visualization. Maria J. S. Costa: Formal analysis, Investigation, Data curation, Writing – original draft, Formal analysis, Writing – review & editing. Renato A. Antunes: Resources, Methodology, Investigation, Writing – review & editing. Raphael O. Ferreira: Formal analysis, Methodology. Rejane M.P. Silva: Formal analysis, Methodology, Writing – review & editing. Reginaldo S. Santos: Conceptualization, Methodology, Writing – review & editing, Supervision, Project administration.

Declaration of competing interest

The authors declare that they have no known competing financial interests or personal relationships that could have appeared to influence the work reported in this paper.

Data availability

No data was used for the research described in the article.

Acknowledgements

The authors would like to thank the research funding agencies CAPES and CNPq. Also, thanks to CCN2-PPGCM-UFPI-LIMAV, FAPESP-CDMF for their technical support.

Appendix A. Supplementary data

Supplementary data to this article can be found online at https://doi.org/10.1016/j.optmat.2023.114081.

References

[1] X. Chen, S.S. Mao, Titanium dioxide nanomaterials: synthesis, properties, modifications and applications, Chem. Rev. 107 (2007) 2891–2959, https://doi.org/10.1021/cr0500535.
[2] H.G. Oliveira, D.C. Nery, C. Longo, Effect of applied potential on photocatalytic phenol degradation using nanocrystalline TiO_2 electrodes, Appl. Catal. B Environ. 93 (2010) (2010) 205–211, https://doi.org/10.1016/j.apcatb.2009.09.030.
[3] K. Rajeshwar, Hydrogen generation at irradiated oxide semiconductor–solution interfaces, J. Appl. Electrochem. 37 (2007) 765–787.
[4] I.C. Carvalho, M.L. Barbosa, M.J.S. Costa, E. Longo, L.S. Cavalcante, V.G.F. Viana, R.S. Santos, TiO_2-based dye-sensitized solar cells prepared with bixin and norbixin natural dyes: effect of 2,2'-bipyridine additive on the current and voltage, Optik 218 (2020), 165236, https://doi.org/10.1016/j.ijleo.2020.165236.
[5] Á. Ágoston, L. Balassa, Á. Deák, G.F. Samu, S.P. Tallósy, G. Gombár, L. Janovák, Photocatalytic and antimicrobial activity of sulfur-functionalized TiO_2 containing composite films, Chem. Eng. Technol. 46 (2023) 927–933, https://doi.org/10.1002/ceat.202200489.
[6] Y.-Y. Wang, Y.-X. Chen, T. Barakat, Y.-J. Zeng, J. Liu, S. Siffert, B.-L. Su, Recent advances in non-metal doped titania for solar-driven photocatalytic/photoelectrochemical water-splitting, J. Energy Chem. 66 (2022) 529–559, https://doi.org/10.1016/j.jechem.2021.08.038.
[7] X. Chen, A. Selloni, Introduction: titanium dioxide (TiO_2) nanomaterials, Chem. Rev. 114 (2014) 9281–9282, https://doi.org/10.1021/cr500422r.
[8] Y. Wang, L. Yin, J. Wu, N. Li, N. He, H. Zhao, X. Li, X. Lai, Q. Wu, Enhanced charge separation efficiency of sulfur-doped TiO_2 nanorod arrays for an improved photoelectrochemical glucose sensing performance, J. Mater. Sci. 57 (2022) 1362–1372, https://doi.org/10.1007/s10853-021-06617-3.
[9] R.V. Nair, V.S. Gummaluri, M.V. Matham, V. C, A review on optical bandgap engineering in TiO_2 nanostructures via doping and intrinsic vacancy modulation towards visible light applications, J. Phys. Appl. Phys. 55 (2022) (2022), 313003, https://doi.org/10.1088/1361-6463/ac6135.
[10] A.M. Alotaibi, S. Sathasivam, B.A.D. Williamson, A. Kafizas, C. Sotelo-Vazquez, A. Taylor, D.O. Scanlon, I.P. Parkin, Chemical vapor deposition of photocatalytically active pure brookite TiO_2 thin films, Chem. Mater. 30 (2018) 1353–1361, https://doi.org/10.1021/acs.chemmater.7b04944.

[11] F.J. Al-Maliki, O.A. Hammadi, B.T. Chiad, E.A. Al-Oubidy, Photocatalytic activity of Ag-doped TiO_2 nanostructures synthesized by DC reactive magnetron co-sputtering technique, Opt. Quant. Electron. 52 (2020) 188, https://doi.org/10.1007/s11082-020-02315-7.

[12] M. Crisan, A. Braileanu, M. Raileanu, M. Zaharescu, D. Cris, N. Dragan, M. Anastasescu, A. Ianculescu, I. Niţoi, V.E. Marinescu, S.M. Hodorogea, Sol-gel S-doped TiO_2 materials for environmental protection, J. Non-Cryst. Solids 354 (2008) 705–711, https://doi.org/10.1016/j.jnoncrysol.2007.07.083.

[13] B.G.T. Keerthana, T. Solaiyammal, S. Muniyappan, P. Murugakoothan, Hydrothermal synthesis and characterization of TiO_2 nanostructures prepared using different solvents, Mater. Lett. 220 (2018) 20–23, https://doi.org/10.1016/j.matlet.2018.02.119.

[14] V.V. Pillai, S.P. Lonkar, S.M. Alhassan, Template-free, solid-state synthesis of hierarchically macroporous S-doped TiO_2 nano-photocatalysts for efficient water remediation, ACS Omega 5 (2020) 7969–7978, https://doi.org/10.1021/acsomega.9b04409.

[15] A.L. da Silva, J. Bettini, A.A. Bernardes, R.H.R. Castro, D. Gouvêa, Improving TiO_2 anatase nanostability via interface segregation: the role of the ionic radius, J. Phys. Chem. C 127 (2023) 1536–1547, https://doi.org/10.1021/acs.jpcc.2c04271.

[16] R.S. Santos, G.A. Faria, C. Giles, C.A.P. Leite, H.D.S. Barbosa, M.A.Z. Arruda, C. Longo, Iron insertion and hematite segregation on Fe-doped TiO_2 nanoparticles obtained from sol-gel and hydrothermal methods, ACS Appl. Mater. Interfaces 4 (2012) 5555–5561, https://doi.org/10.1021/am301444k.

[17] S.A. Bakar, C.A. Ribeiro, Comparative run for visible-light-driven photocatalytic activity of anionic and cationic S-doped TiO_2 photocatalysts: a Case study of possible sulfur doping through chemical protocol, J. Mol. Catal. Chem. 421 (2016) 1–15, https://doi.org/10.1016/j.molcata.2016.05.003.

[18] A.V. Vorontsov, H. Valdés, Insights into the visible light photocatalytic activity of S-doped hydrated TiO_2, Int. J. Hydrogen Energy 44 (2019) 17963–17973, https://doi.org/10.1016/j.ijhydene.2019.05.103.

[19] A. Piatkowska, M. Janus, K. Szymanski, S. Mozia, C-N- and S-Doped TiO_2 photocatalysts: a review, Catalyst 11 (2021) 144, https://doi.org/10.3390/CATAL11010144.

[20] N. Sharotri, S. Gupta, D. Sud, Visible light responsive S-Doped TiO_2 nanoparticles: synthesis, characterization and photocatalytic degradation of pollutants, Nanotechnol. Environ. Eng. 7 (2022) 503–515, https://doi.org/10.1007/s41204-022-00228-2.

[21] S. Cravanzola, F. Cesano, F. Gaziano, D. Scarano, Sulfur-doped TiO_2: structure and surface properties, Catalysts 7 (2017) 214, https://doi.org/10.3390/catal7070214214.

[22] P. Basera, S. Saini, E. Arora, A. Singh, M. Kumar, S. Bhattacharya, Stability of non-metal dopants to tune the photo-absorption of TiO_2 at realistic temperatures and oxygen partial pressures: a hybrid DFT study, Sci. Rep. 9 (2019), https://doi.org/10.1038/s41598-019-47710-7.

[23] R.T. Bento, O.V. Correa, M.F. Pillis, Photocatalytic activity of undoped and sulfur-doped TiO_2 films grown by MOCVD for water treatment under visible light, J. Eur. Ceram. Soc. 39 (2019) 3498–3504, https://doi.org/10.1016/j.jeurceramsoc.2019.02.046.

[24] T. Umebayashi, T. Yamaki, H. Itoh, K. Asai, Band gap narrowing of titanium dioxide by sulfur doping, Appl. Phys. Lett. 81 (2002) 454–456, https://doi.org/10.1063/1.1493647.

[25] T. Umebayashi, T. Yamaki, S. Tanaka, K. Asai, Visible light-induced degradation of methylene blue on S-doped TiO_2, Chem. Lett. 32 (2003) 330–331, https://doi.org/10.1246/cl.2003.330.

[26] F. Wang, F. Li, L. Zhang, H. Zeng, Y. Sun S. Zhang, X. Xu, $STiO_2$ with enhanced visible-light photocatalytic activity derived from TiS_2 in deionized water, Mater. Res. Bull. 87 (2017) 20–26, https://doi.org/10.1016/j.materresbull.2016.11.014.

[27] H. Jing, Q. Cheng, J.M. Weller, X.S. Chu, Q.H. Wang, C.K. Chan, Synthesis of TiO_2 nanosheet photocatalysts from exfoliation of TiS_2 and hydrothermal treatment, J. Mater. Res. 33 (2018) 3540–3548, https://doi.org/10.1557/jmr.2018.165.

[28] G. Meunier, R. Dormoy, A. Levasseur, New amorphous titanium oxysulfides obtained in the form of thin films, Thin Solid Films 205 (1991) 213–217, https://doi.org/10.1016/0040-6090(91)90302-E.

[29] L.A.C. Smith, M.L. Trudeau, M. Provencher, M.E. Smith, D.M. Antonelli, Low-temperature synthesis and electrochemical properties of mesoporous titanium oxysulfides, Chemelectrochem 3 (2016) 256–265, https://doi.org/10.1002/celc.201500463.

[30] J.G.A. van Kasteren, S.B. Basuvalingam, M. Mattinen, A.E.A. Bracesco, W.M. M. Kessels, A.A. Bol, B. Macco, Growth mechanism and film properties of atomic-layer-deposited titanium oxysulfide, Chem. Mater. 34 (2022) 7750, https://doi.org/10.1021/acs.chemmater.2c01033.

[31] M.J.S. Costa, G.S. Costa, A.E.B. Lima, G. Eduardo da Luz Júnior, E. Longo, L. S. Cavalcante, R.S. Santos, Photocurrent response and progesterone degradation by employing WO_3 films modified with platinum and silver nanoparticles, ChemPlusChem 83 (2018) 1153–1161, https://doi.org/10.1002/cplu.201800534.

[32] G.S. Costa, M.J.S. Costa, H.G. Oliveira, L.C.B. Lima, G.E. Luz Jr., L.S. Cavalcante, R. S. Santos, Effect of the applied potential condition on the photocatalytic properties of $Fe_2O_3|WO_3$ heterojunction films, J. Inorg. Organomet. Polym. Mater. 30 (2020) 2851–2862, https://doi.org/10.1007/s10904-019-01429-0.

[33] J.P.C. Moura, R.Y.N. Reis, A.E.B. Lima, R.S. Santos, G.E. Luz, Improved photoelectrocatalytic properties of ZnO/$CuWO_4$ heterojunction film for RhB degradation, J. Photochem. Photobiol. Chem. 401 (2020), 112778, https://doi.org/10.1016/j.jphotochem.2020.112778.

[34] M.J.S. Costa, G.S. Costa, A.E.B. Lima, G.E. Luz Jr., E. Longo, L.S. Cavalcante, R. S. Santos, Investigation of charge recombination lifetime in γ-WO_3 films modified with Ag^0 and Pt^0 nanoparticles and its influence on photocurrent density, Ionics 24 (2018) 3291–3297, https://doi.org/10.1007/s11581-018-2640-1.

[35] R.Y.N. Reis, A.E.B. Lima, M.J.S. Costa, J.F. Cruz-Filho, J.P.C. Moura, R.S. Santos, G. E. Luz Jr., Enhanced photoelectrocatalytic performance of ZnO films doped with N_2 by a facile electrochemical method, Surface. Interfac. 21 (2020), 100675, https://doi.org/10.1016/j.surfin.2020.100675.

[36] S. Prabakar, C.W. Bumby, R.D. Tilley, Liquid-phase synthesis of flower-like and flake-like titanium disulfide nanostructures, Chem. Mater. 21 (2009) 1725–1730, https://doi.org/10.1021/cm900110h.

[37] S. Landi, I.R. Segundo, E. Freitas, M. Vasilevskiy, J. Carneiro, C.J. Tavares, Use and misuse of the Kubelka-Munk function to obtain the band gap energy from diffuse reflectance measurements, Solid State Commun. 341 (2022), 114573, https://doi.org/10.1016/j.ssc.2021.114573.

[38] C. Larquet, S. Carenco, Metal oxysulfides: from bulk compounds to nanomaterials, Front. Chem. 8 (2020) 179, https://doi.org/10.3389/fchem.2020.00179.

[39] D. Gonbeau, C. Guimon, G. Pfister-Guillouzo, A. Levasseur, G. Meunier, R. Dormoy, XPS study of thin films of titanium oxysulfidesSurf, Scipolicy 254 (1991) 81–89, https://doi.org/10.1016/0039-6028(91)90640-E.

[40] B.J. Matsoso, K. Ranganathan, B.K. Mutuma, T. Lerotholi, G. Jones, N.J. Coville, Synthesis and characterization of boron carbon oxynitride films with tunable composition using methane, boric acid and ammonia, New J. Chem. 41 (2017) 9497–9504, https://doi.org/10.1039/C7NJ01886J.

[41] B. Bharti, S. Kumar, H.N. Lee, R. Kumar, Formation of oxygen vacancies and $Ti^{(3+)}$ state in TiO_2 thin film and enhanced optical properties by air plasma treatment, Sci. Rep. (2016), 32355, https://doi.org/10.1038/2Fsrep32355.

[42] T. Cottineau, A. Rouet, V. Fernandez, M. Richard-Plouet, Intermediate band in the gap of photosensitive hybrid gel based on titanium oxide: role of coordinated ligands during photoreduction, J. Mater. Chem. A. 2 (2014) 11499–11508, https://doi.org/10.1039/C4TA02127D.

[43] A. Baszczuk, M. Jasiorski, M. Winnicki, Low-temperature transformation of amorphous sol–gel TiO_2 powder to anatase during cold spray deposition, J. Therm. Spray Technol. 27 (2018) 1551–1562, https://doi.org/10.1007/s11666-018-0769-0.

[44] M. Catauro, E. Tranquillo, G. Dal Poggetto, M. Pasquali, A. Dell'Era, S. Vecchio, Ciprioti Influence of the heat treatment on the particles size and on the crystalline phase of TiO_2 synthesized by the sol-gel method, Materials 11 (2018) 2364, https://doi.org/10.3390/ma11122364.

[45] T. Sekiya, S. Ohta, M. Kamei, S. Hanakawa, Kurita Raman spectroscopy and phase transition of anatase TiO_2 under high pressure, J. Phys. Chem. Solid. 62 (2001) 717–721, https://doi.org/10.1016/S0022-3697(00)00229-8.

[46] E.J. Ekoi, A. Gowen, R. Dorrepaal, D.P. Dowling, Characterisation of titanium oxide layers using Raman spectroscopy and optical profilometry: influence of oxide properties, Results Phys. 12 (2019) 1574–1585, https://doi.org/10.1016/j.rinp.2019.01.054.

[47] M.J.S. Costa, A.E.B. Lima, E.P. Ribeiro, G.S. Costa, E. Longo, G.E. Luz Jr., L. aecio Santos Cavalcante, Reginaldo da Silva Santos, Transition metal tungstates AWO_4 (A^{2+} = Fe, Co, Ni, and Cu) thin films and their photoelectrochemical behavior as photoanode for photocatalytic applications, J. Appl. Electrochem. (2023), https://doi.org/10.1007/s10800-023-01851-w.

[48] S. Sodergren, A. Hagfeldt, J. Olsson, S.-E. Lindquist, Theoretical models for the action spectrum and the current-voltage characteristics of microporous semiconductor films in photoelectrochemical cells, J. Phys. Chem. 98 (1994) 5552–5556, https://doi.org/10.1021/j100072a023.

[49] A. Hangfeld, M. Grätzel, Light-induced redox reactions in nanocrystalline systems, Chem. Rev. 95 (1995) 49–68, https://doi.org/10.1021/cr00033a003.